UC Berkeley
UC Berkeley Previously Published Works

Title
Dynamic Structure and Phase Behavior of a Block Copolymer Electrolyte under dc Polarization

Permalink
https://escholarship.org/uc/item/0gb0b7nc

Journal
ACS Applied Materials & Interfaces, 12(51)

ISSN
1944-8244

Authors
Galluzzo, Michael D
Loo, Whitney S
Schaible, Eric
et al.

Publication Date
2020-12-23

DOI
10.1021/acsami.0c16209

Peer reviewed

Dynamic Structure and Phase Behavior of a Block Copolymer Electrolyte under Dc Polarization

Michael D. Galluzzo[1,2], Whitney S. Loo[1], Eric Schaible[3], Chenhui Zhu[3], and Nitash P. Balsara[1,2,4]*

[1]Department of Chemical and Biomolecular Engineering University of California, Berkeley, CA 94720, United States.

[2]Materials Science Division, Lawrence Berkeley National Laboratory, Berkeley, CA 94720, United States

[3]Advanced Light Source, Lawrence Berkeley National Laboratory, Berkeley, CA 94720, United States

[4]Joint Center for Energy Storage Research (JCESR), Lawrence Berkeley National Laboratory, Berkeley, CA 94720, United States.

KEYWORDS

concentration hotspots, composite electrolytes, block copolymer, gyroid, dc polarization, lithium metal

AUTHOR INFORMATION

Corresponding Author

* Correspondence to: nbalsara@berkeley.edu

ABSTRACT

An important consideration when designing lithium battery electrolytes for advanced applications is how the electrolyte facilitates ion transport at fast charge and discharge rates. Large current densities are accompanied by large salt concentration gradients across the electrolyte. Nanostructured composite electrolytes have been proposed to enable the use of high energy density lithium metal anodes, but many questions about the interplay between the electrolyte morphology and the salt concentration gradient that forms under dc polarization remain unanswered. To address these questions, we use an *in situ* small angle X-ray scattering technique to examine the nanostructure of a polystyrene-*block*-poly(ethylene oxide) copolymer electrolyte under dc polarization with spatial and temporal resolution. In the quiescent state, the electrolyte exhibits a lamellar morphology. The passage of ionic current in a lithium symmetric cell leads to the formation of concurrent phases: a disordered morphology near the negative electrode, lamellae in the center of the cell, and coexisting lamellae and gyroid near the positive electrode. The most surprising result of this study was obtained after the applied electric field was turned off: a current-induced gyroid phase grows in volume for six hours in spite of the absence of an obvious driving force. We show that this reflects the formation of localized pockets of salt-dense electrolyte, termed concentration hotspots, under dc polarization. Our methods may be applied to understand the dynamic structure of composite electrolytes at appreciable current densities.

MAIN TEXT

Introduction

There are many challenges associated with designing rechargeable batteries that offer increased performance over the current state of the art in lithium-ion technology. From the perspective of the electrolyte, one must address two critical design goals: 1) ensure compatibility with high energy density electrode materials[1,2], and 2) enable ion transport at rates required by the application[3]. There is considerable interest in developing new composite electrolytes to meet these goals. Multiple phases with different material properties are leveraged to obtain an electrolyte with orthogonal properties (*e.g.* compatibility with lithium metal anodes and high ionic conductivity). Examples include ceramic nanoparticles dispersed in an ion conducting matrix[4], block copolymers with co-continuous ion conducting and rigid domains[5], and crosslinked polymer gels swollen with an electrolyte solution[6]. In homogeneous electrolyte systems (*i.e.*, a mixture of a salt in a single solvent), the second law of thermodynamics requires that passing ionic current result in a monotonic salt concentration profile between the electrodes when the electrolyte is initially uniform in concentration. There are, however, many unanswered questions about the interplay between morphology and concentration gradients in multiphase systems wherein ion transport is fundamentally different in the two phases. Passing current through these electrolytes can lead to rearrangement of phases or the formation of new structures that are not present in the quiescent state[7]. In principle, composite electrolytes can exhibit salt concentration hotspots, *i.e.,* pockets where the local salt concentration exceeds the nominal value due to transport bottlenecks. Our understanding of these phenomena is limited.

The rearrangement of phases in a composite electrolyte is a natural consequence of dc polarization because the structure of composite electrolytes often varies with salt concentration[8–11]. Concentration gradients emerge across the electrolyte when the mobility of the anion is non-zero[12]. At early times, the gradients are localized near the electrodes and the salt concentration in the middle of the cell remains more or less unchanged. With time, the gradients propagate toward the middle of the cell until a time-invariant concentration profile is achieved. Consequently, the rearrangement of phases will depend on both distance from the electrode and time. Additional complexities may arise due to concentration hotspots. We note that these phenomena are also relevant for standard lithium ion battery components which inherently consist of multiple phases: the electrodes are comprised of active particles mixed with electrolyte, and ion transport between the electrodes occurs within the pores of an inert separator wetted with electrolyte.

The composite electrolyte system studied in this work is a polystyrene-*block*-poly(ethylene oxide) (SEO) with bis(trifluoromethylsulfonyl)amine lithium salt (LiTFSI) where glassy polystyrene (PS) provides mechanical rigidity and poly(ethylene oxide) (PEO) solvates the lithium salt and enables ion conduction. The development of concentration gradients in SEO/LiTFSI mixtures can be predicted using concentrated solution theory because ionic conductivity, salt diffusion coefficient, cation transference number with respect to the solvent velocity, and thermodynamic factor have been measured as a function salt concentration[13,14]. However, concentrated solution theory does not account for the rearrangement of phases or phase transitions. Our purpose is to study the effect of applied current on the morphology and phase behavior of an SEO/LiTFSI electrolyte. We track the rearrangement of phases and phase

transitions that occur in this electrolyte during polarization by *in situ* small angle X-ray scattering (SAXS) experiments. These experiments enable determination of the local structure of the electrolyte as a function of time and distance from the electrodes. The equilibrium lamellar phase gives way to a disordered phase near the negative electrode and small pockets of a gyroid phase near the positive electrode. The most surprising result of this study was obtained after the applied field was turned off: the current-induced gyroid phase grows in volume for six hours in spite of the absence of an obvious driving force.

Experimental Methods

We designed a custom electrochemical cell (shown schematically in Figure 1a) to enable structural characterization of the electrolyte during polarization via SAXS measurements. The cell was held in a 2 mm thick polyether ether ketone (PEEK) component with a rectangular channel cut through. Lithium metal was pressed on one face of two stainless-steel blocks that served as current collectors and were then inserted into the channel resulting in a 1.23 mm gap between the two lithium electrodes. The active face of the stainless-steel block/lithium metal assembly had dimensions of 1.95 mm by 3.95 mm and the lithium was approximately 100 μm thick. The polymer electrolyte was then hot pressed into the resulting gap with Kapton windows affixed over the exposed faces. Cell assembly was performed in an argon-filled glove box with less than 1 ppm O_2 and H_2O levels. The entire cell was sealed in an aluminum laminated pouch with nickel tabs secured to the stainless-steel blocks protruding out to allow electrical connections. The cell was then removed from the glove box and affixed to a custom-built heat stage for testing. The nickel tabs were attached to a Biologic VMP3 potentiostat for electrochemical measurements. A picture of the assembled cell before pouch sealing is shown in

Figure S1. The orientation of the cell was such that the X-ray beam passed parallel to the electrodes, passing through the cell components in the following order: pouch, Kapton, 1.95 mm of electrolyte, Kapton, and pouch. All SAXS data was obtained at beamline 7.3.3. of the Advanced Light Source (ALS) at Lawrence Berkeley National Laboratory[15]. The size of the beam was approximately 700 μm x 300 μm. We oriented the cell such that the 700 μm dimension was parallel to the electrode and the 300 μm dimension was perpendicular. The X-ray beam was then scanned between the two electrodes with the optimal spatial resolution considering the electrolyte thickness, $L = 1.23$ mm, and beam dimensions. Previous studies have been conducted with the X-ray beam oriented perpendicular to the electrodes, resulting in scattering data averaged over the entire length of the electrolyte[7,16]. To our knowledge, this is the first report of an X-ray scattering experiment performed on a block copolymer electrolyte under dc polarization with spatial and temporal resolution.
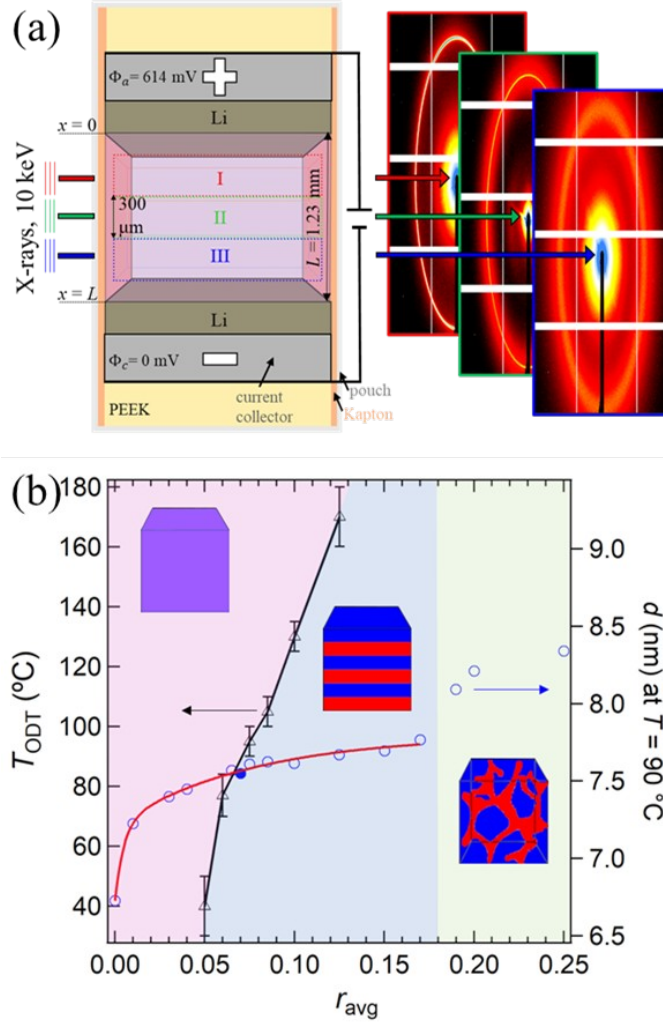
Figure 1. (a) Schematic representation of the experimental set up. 10 keV X-rays pass perpendicular to the direction of ion motion (parallel to the lithium electrodes), sampling three distinct regions of the electrolyte (pink shaded region) which are directly adjacent to each other. Region I, II, and III are centered at $x L^{-1}$ = 0.24, 0.50, and 0.74, as shown by the dashed boxes and the beam dimension in the x-direction is 300 μm. Based on the cell polarity, the salt concentration of Region I increases and Region III decreases during polarization. Representative 2D SAXS patterns are shown for each region (corresponding to t = 7 h). (b) Phase diagram of the polymer electrolyte SEO(1.7-1.4)/LiTFSI used in this study. The order-to-disorder transition temperature (T_{ODT}) versus salt concentration, r_{avg}, is plotted with triangle markers on the left axis; r_{avg} = [LiTFSI]/[EO]. Shaded regions indicate the phases observed at each temperature and r_{avg}, where pink, blue, and green correspond to the disordered, lamellar, and gyroid morphologies, respectively. The domain spacing, d, versus r_{avg} at 90°C is plotted on the right axis as open circle markers. The filled circle represents the sample used for this study (r_{avg} = 0.07) which exhibits a

lamellar morphology but is near the disordered/lamellar phase boundary. Data points with open markers were taken from refs 7, 8. The red line is a fit given by Equation 1.

Results and Discussion

Phase Behavior of the Electrolyte in the Quiescent State

The electrolyte was comprised of a linear SEO diblock copolymer with a 1.7 kg mol^{-1} PS block and 1.4 kg mol^{-1} PEO block mixed with LiTFSI. The molar ratio of LiTFSI molecules to ether oxygens, $r_{avg} = \frac{[LiTFSI]}{[EO]}$, was 0.07. We use the subscript 'avg' to denote that this is the average salt concentration for the entire electrolyte, which must be conserved throughout the experiment. When a dc potential is applied across the cell, salt accumulates at the positive electrode (where the anodic reaction, Li^0 → Li$^+$ + e$^-$, occurs) and is depleted at the negative electrode (where the cathodic reaction, Li$^+$ + e$^-$ → Li^0, occurs), which results in a gradient in the local salt concentration, $r(x, t)$. We define the x-coordinate such that $x = 0$ at the anode (positive electrode) and $x = L$ at the cathode (negative electrode). Salt concentration gradients have been measured experimentally in homogeneous electrolytes[17–20]. For a microstructured (*i.e.* inhomogeneous) block copolymer electrolyte, there is the additional complication that morphology will depend on the local salt concentration.

We present the phase behavior of the SEO copolymer as a function of r_{avg} in Figure 1b. The addition of salt to a block copolymer affects the morphology, conducting phase volume fraction (f_c), and domain spacing, relative to the neat state[8,11,21,22]. The phase behavior of the SEO copolymer doped with different amounts of salt was characterized by conventional SAXS experiments in inert sample holders. At low salt concentrations, *i.e.* $r_{avg} < 0.05$, the sample is

disordered (DIS) at all temperatures ($T > 40°C$). Increasing salt concentration results in a phase transition to an ordered lamellar (LAM) phase. The order-to-disorder transition temperature (T_{ODT}) increases with r_{avg}. We plot T_{ODT} as a function of r_{avg} on the left axis of Figure 1b as open triangles. When r_{avg} exceeds 0.17, the lamellar phase gives way to a gyroid (GYR) morphology, regardless of temperature. The disordered-to-lamellar-to-gyroid transitions are driven by changes in polymer/salt interactions[23] and changes in f_c. As r_{avg} is increased from 0 to 0.25, f_c increases from 0.44 to 0.58. The shaded regions and cartoon schematics in Figure 1b represent the morphology in the designated temperature and salt concentration windows. SAXS data from this system contains a primary SAXS peak at $q = q^i$, where q is the magnitude of the scattering vector. On the right axis in Figure 1b, we plot the domain spacing, d, as a function of salt concentration at 90°C as circles ($d = \dfrac{2\pi}{q^i}$). Data plotted with open symbols (circles and triangles) in Figure 1b was taken from Refs 7,8. The closed symbol represents the sample used in this study. The disordered state (DIS) is characterized by fluctuations in the local density of styrene and ethylene oxide monomer units with a characteristic spacing between fluctuations, d_{DIS}, but no long-range order. The lamellar morphology (LAM) is characterized by alternating 2D PS- and PEO-rich domains where the characteristic distance, d_{LAM}, is the distance between the center of two lamella of the same component. The gyroid morphology (GYR) is characterized by 3D network of a minority component (PS) dispersed in a matrix of the majority component (PEO) with a characteristic spacing, d_{GYR}. From the neat state (*i.e.*, $r_{avg} = 0$) to $r_{avg} = 0.04$, d_{DIS} increases rapidly from 6.73 nm to 7.45 nm. Above $r_{avg} = 0.04$, d increases slowly and smoothly across the

disordered to lamellar transition with d_{LAM} = 7.78 nm at r_{avg} = 0.17. The domain spacing for the

disordered and lamellar morphologies is well-described by a double exponential function:

$$d = 7.80 - 0.585 \exp[-13.3 \, r_{avg}] - 0.486 \exp[-210 \, r_{avg}] \tag{1}$$

shown as a red curve in Figure 1b and applies for $0 \leq r_{avg} \leq 0.15$. For $r_{avg} > 0.17$, the transition

from lamellar to gyroid is accompanied by a discontinuous change in the dependence of domain

spacing on salt concentration, with d_{GYR} = 8.09 nm at r_{avg} = 0.19 and reaching 8.34 nm at r_{avg} =

0.25.

Phase Behavior of the Electrolyte under Dc Polarization

The electrolyte was loaded into the cell shown in Figure 1a and subjected to a constant

potential of 500 mV mm^{-1} beginning at time t = 0 h. Based on the thickness of cell (L = 1.23

mm), the applied potential translates to an anodic potential, Φ_a = 614 mV; the cathodic potential,

Φ_c, is defined to be zero. In a practical battery electrolyte, L is on the order of 10 μm, which

corresponds to a potential drop of 5 mV across the electrolyte. While the cell thickness is much

larger than a practical battery electrolyte, the behavior we observe will be analogous in thinner

membranes at the same $\Delta\Phi / L$ or iL, where $\Delta\Phi$ is the potential drop across the electrolyte and i

is the current density.

The SEO electrolyte with r_{avg} = 0.07 used in this experiment is represented by a filled

blue circle in Figure 1b; it has a lamellar morphology but is near the DIS-LAM phase boundary.

To monitor the structure of the polymer in response to the applied field, we sample three regions

of the cell. Region I, II, and III are centered at $x \, L^{-1}$ = 0.26, 0.50, and 0.74, respectively, and

spaced by 300 μm, as shown in Figure 1a. We use the notation r_I, r_{II}, and r_{III} to denote the

average salt concentration in each region. Before polarization, the sample was heated to 120 °C to access the disordered state and erase any thermal history before cooling to 90°C to run the experiment. We have established that lithium is prone to dissolve from the electrode at elevated temperatures (>90 °C)[24], so we limited the annealing step to 20 min at 120 °C. In Figure 2a-c, we present the azimuthally averaged 1D SAXS intensity as a function of q for the three regions. The black curve in each plot (t = -0.1 h) represents the structure after cooling to 90 °C and before polarization. The sharp scattering peak at q^{i} = 0.83 nm^{-1} and higher order scattering peak at $2q^{i}$ = 1.6 nm^{-1} is indicative of the lamellar morphology. The red curves represent data taken during polarization at 500 mV mm^{-1}, and the blue curves represent the data taken after the cell was switched to open circuit at t = 8.3 h. The time stamp on the curves in Figure 2c apply to Figure 2a-c. A total of 86 measurements were made for each region over the course of the experiment, and the selected curves in Figure 2a-c highlight the observed phase transitions.
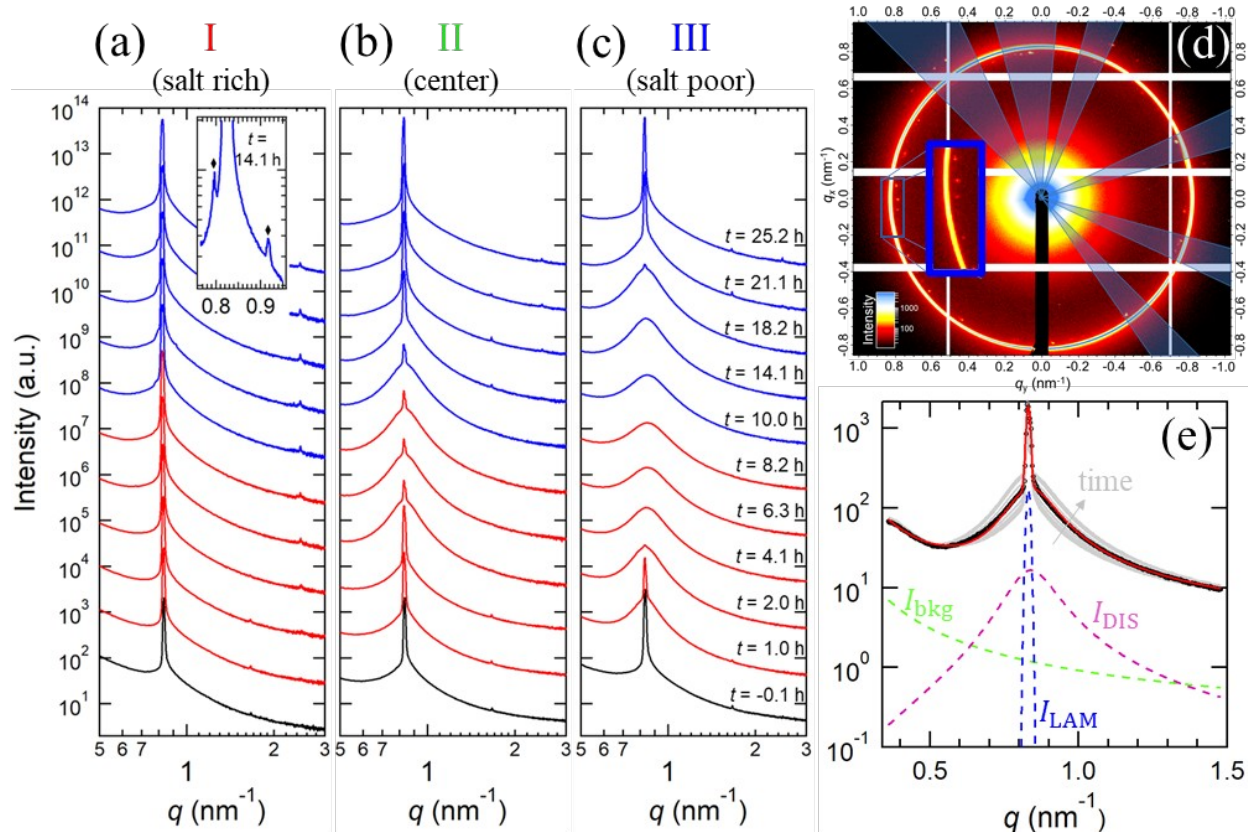
Figure 2. Azimuthally averaged SAXS profiles as a function of time for (a) Region I, near the positive (salt rich) electrode, (b) Region II, near the middle of the cell, and (c) Region III, near the negative (salt poor) electrode. Black curves represent the initial morphology taken before polarization. Red curves indicate the morphology during polarization at 500 mV/mm. Blue curves indicate the morphology after the cell is switched to open circuit at $t = 8.3$ h. The inset in (a) highlights the emergent peak corresponding to the gyroid morphology with Bragg reflections at $q_{GYR}^{\'}$ and $\sqrt{4/3}\,q_{GYR}^{\'}$ (diamond markers). (d) 2D SAXS pattern of Region I at $t = 14.1$ h. The ring corresponds to the primary scattering peak of the lamellar phase. The scattered spots directly inside of the ring correspond to $q_{GYR}^{\'}$ (magnified in the inset) and the spots outside of the ring correspond to the $\sqrt{4/3}\,q_{GYR}^{\'}$ reflection. The highlighted sectors were selectively averaged to characterize scattering from the gyroid phase. (e) 1D plots of $I(q)$ for Region II from $t = 0.8$ h to $t = 4.8$ h (gray curves). $I(q)$ at $t = 2.6$ h is plotted with black open circles and the red curve is a fit of Equation 2 to the data. The fit is deconvoluted into three parts and offset by a decade for clarity: background (green dashed line), broad disordered peak (purple dashed line), and sharp ordered peak (blue dashed line).

Near the negative electrode (Region III, Figure 2c), the sharp scattering peak seen at t = -0.1 h and t = 1.0 h is replaced by a broad scattering peak characteristic of a disordered phase that persists through the polarization step (up to t = 8.2 h). It is evident that the block copolymer electrolyte in Region III undergoes an order-to-disorder transition. After the field is turned off at t = 8.3 h, the sharp scattering peak characteristic of the lamellar phase is recovered. Near the center of the cell (Region II, Figure 2b), a similar trend is observed, however at t = 8.2 h, the scattering profile contains signatures of both ordered and disordered domains. As was the case in Region III, the lamellar phase is recovered after the cell is switched to open circuit. Near the positive electrode (Region I, Figure 2a), the ordered lamellar phase persists throughout polarization ($0 < t$ (h) < 8.3). At t = 8.2 h (near the end of the 500 mV mm^{-1} polarization step), a small peak emerges on the low-q side of the primary peak. As time progresses, an additional peak emerges on the high-q side. The diamond markers in the inset of Figure 2a denote these two peaks at q = 0.796 and 0.918 nm^{-1}, respectively.

The 2D SAXS pattern from Region I at t = 14.1 h is presented in Figure 2d. The primary scattering peak corresponding to the lamellar phase in the 1D plot is represented by the narrow, continuous ring of high intensity. The small peaks on either side of the primary lamellar peak in the 1D plot correspond to the spots of high intensity inside and outside of the bright ring in the 2D image. These spots are highlighted in the inset of Figure 2d. The azimuthal angles of the spots do not change during the course of the experiment. While the spots are clear in the 2D image, they are not well resolved when the 2D scattering intensity profile is azimuthally averaged. To achieve better resolution, we averaged selected sectors of the 2D scattering profiles which are indicated by the shaded regions in Figure 2d. An example of the resulting 1D profile is

shown as an inset in Figure 2a. In addition to the scattering peak corresponding to the lamellar phase, we observe peaks at $q_{GYR}^{\ddot{\imath}}= 0.796$ nm^{-1} and $\sqrt{4/3}\,q_{GYR}^{\ddot{\imath}} = 0.918$ nm^{-1}. These peaks are standard signatures of the gyroid morphology in block copolymers[7,25,26] and this morphology coexists with the lamellar morphology in Region I.

To track the phase transitions observed in Figure 2a-c, we fit the scattering data, $I(q)$ for $0.36 < q$ (nm^{-1}) < 1.48 to Equation 2:[27]

$$I(q)=I_{DIS}(q)+I_{LAM}(q)+I_{bkg}(q), \tag{2}$$

where $I_{DIS}(q)$, $I_{LAM}(q)$, and $I_{bkg}(q)$ account for the scattering from the disordered phase, lamellar phase, and background, respectively. (The scattered intensity from the gyroid phase in Region I is much smaller than the lamellar phase, so we neglect it in the fit.) I_{DIS} is given by the Liebler structure factor[28], I_{LAM} is a Gaussian function, and I_{bkg} is a decaying exponential. The details of the fit are discussed in the Supporting Information. The gray curves in Figure 2e represent the raw data from Region II from $t = 0.8$ h to $t = 4.8$ h and the raw data at $t = 2.6$ h is plotted as black data points. We use the $t = 2.6$ h scattering profile to describe our fitting procedure. The solid red line in Figure 2e represents the fit of Equation 2 and three contributions to $I(q)$, I_{DIS} (purple), I_{LAM} (blue), and I_{bkg} (green) are shown by dashed curves that are offset by a decade for clarity. These fits were repeated for all of the scattering profiles obtained from Region I, II, and III. When the sample is completely disordered (*e.g.* $t = 6.3$ h in Figure 2c), we set $I_{LAM} = 0$. For the scattering from the SEO/LiTFSI electrolyte in the quiescent state (*i.e.*, $t = -0.1$ h in Figure 2c), our fitting procedure results in a finite I_{DIS} contribution. In other words, the sharp Gaussian function presented in Figure 2e does not account for all of the scattering seen from the nominally ordered sample. Our sample is in the weak segregation limit and, with the

presence of salt, the Gibbs phase rule requires a coexistence window between the lamellar and disordered phase[29]. In other words, there must be a range of salt concentrations where the equilibrium morphology of the SEO/LiTFSI electrolyte consists of coexisting lamellae and disordered grains. The coexistence in this sample was predicted from theory in Ref [30] and confirmed experimentally in Ref [27]. Given the proximity of our sample (with $r_{avg} = 0.07$) to the order-disorder phase boundary, we interpret the diffuse scattering at the base of the primary peak to indicate coexistence of a disordered phase with the ordered lamellar phase. We certainly expect ordered and disordered phases to exist simultaneously as the sample undergoes an order-to-disorder transition due to salt depletion near the negative electrode. The scattering signatures of the disordered phase emerge smoothly from the diffuse scattering at the base of the primary peak when the cell is polarized (see gray curves in Figure 2e). With increasing time (in the range $0.8 < t$ (h) < 4.8), the I_{DIS} contribution to $I(q)$ increases in Region II.
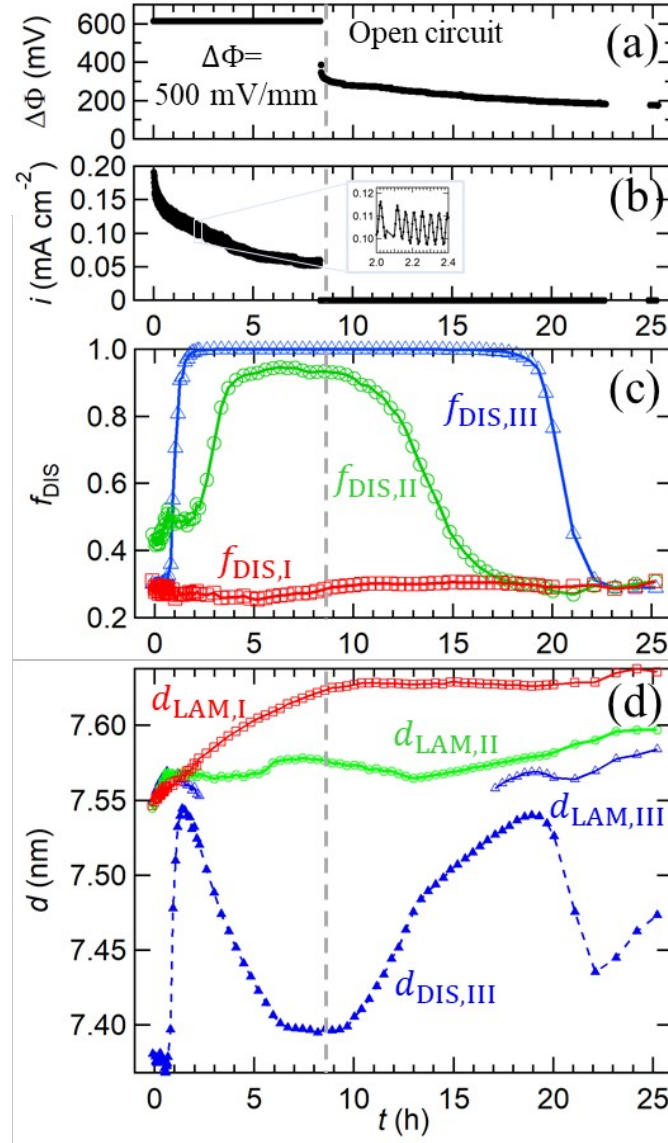
Figure 3. (a) Cell potential drop, $\Delta\Phi$, versus time, t. (b) Current density, i, versus t. From $t = 0$ to $t = 8.3$ h, a constant potential of 614 mV (500 mV mm^{-1}) is applied across the cell and the current is measured. At $t = 8.3$ h (represented by a vertical dashed line), the current is set to zero and the potential is measured. The noise in the voltage and current data is due to interference from the heating stage, shown in the inset of (b). (c) Volume fraction of the disordered phase, f_{DIS}, versus t for Regions I (red squares), II (green circles), and III (blue triangles). (d) Domain spacing of the lamellar phase, d_{LAM}, (open symbols) for Regions I, II, and III and domain spacing of the disordered phase for Region III, d_{DIS} (filled symbols) as a function of time.

The time dependence of cell potential drop, $\Delta\Phi = \Phi_a - \Phi_c$, and current density, i, are

presented in Figure 3a and 3b, respectively. A constant potential, $\Delta\Phi = 623$ mV (500 mV mm^{-1}),

16

was applied across the cell for $0 < t$ (h) < 8.33 during which time the current density, i, was measured. At $t = 8.3$ h, the cell was switched to open circuit ($i = 0$ mA cm^{-2} for $8.3 < t$ (h) < 25.2) and the open circuit potential was recorded. The bulk and interfacial resistance of the cell was measured at intervals spaced by 0.5 h. Similar values were obtained at the beginning and end of the experiment (see Figure S3 of the Supporting Information). The noise in the current and voltage data (inset of Figure 3b highlights an example) is due to interference from the power cycle of the heating stage and could not be avoided. The gray dashed line in Figure 3a-d represents the switch from chronoamperometry to open circuit. In order to quantify the extent of the salt concentration-induced order-to-disorder and disorder-to-order transitions, we calculated the scattering invariants (see Supporting Information for details) of the disordered and lamellar phases (Q_{DIS} and Q_{LAM}, respectively) from the fits described in the preceding paragraph[27,31]. We then calculated the disordered phase volume fraction, f_{DIS}, for Region I, II, and III as a function of time by:

$$f_{DIS} = \frac{Q_{DIS}}{Q_{DIS} + \alpha Q_{LAM}} \text{ ,} \tag{3}$$

where α is a correction factor that accounts for the anisotropic scattering of lamellar grains and the presence of LiTFSI. While all of the scattering from the isotropic disordered phase reaches the detector, lamellar grains with normal orientation along the path of the X-ray beam do not contribute to the scattering signal. During a phase transition, the local salt concentration in the ordered domain will not be equal to that in the disordered domain[27], instead it is the chemical potential of the salt that is equilibrated between the two phases. In principle, α will be a function of both the salt concentration in the ordered domain and disordered domain, both of which change with time in our system. We make the simplification that α does not depend on r and

estimate α = 2.4, which we use for all calculations of f_{DIS}. Our methodology for estimating α is given in the Supporting Information.

We present f_{DIS} as a function of time for Region I (red squares), Region II (green circles), and Region III (blue triangles) in Figure 3c. In Region I, $f_{DIS,I}$ remains fixed at about 0.30, the lowest value seen in our experiment, for the duration of the experiment. Near the positive electrode (Region I), we expect polarization to result in an increase in salt concentration, *i.e.* $r_I > r_{avg}$. Since the sample is ordered in the quiescent state at $r = r_{avg}$ and because the addition of salt stabilizes the ordered phase (Figure 1b), we expect this region to remain ordered during polarization. In Region III, $f_{DIS,III}$ = 0.30 until t = 0.6 h when f_{DIS} begins to increase sharply. At t = 1.8 h, $f_{DIS,III}$ = 0.98 and the region is almost completely disordered. Near the negative electrode, we expect polarization to result in a decrease in salt concentration, i.e. $r_{III} < r_{avg}$, resulting in the disordering of Region III based on the phase diagram presented in Figure 1b. Near the center of the cell (Region II), we expect $r_{II} \approx r_{avg}$ due to the constraint that the average salt concentration in the electrolyte must be constant throughout the experiment. Unlike Region I and III, $f_{DIS,II}$ = 0.45 at t = -0.1 h. Prior to polarization, we expect no difference in the morphology of Regions I, II, and III. We attribute this to subtle differences in the ordered morphology across a 1.23 mm wide sample due to effects such as non-uniformity of sample temperature or an inhomogeneous stress distribution from the electrodes and sample holder. In Region II, $f_{DIS,II}$ increases in two steps. It first increases from 0.45 to 0.49 over the first hour and approaches a short plateau. The second step occurs at t = 2.1 h: $f_{DIS,II}$ begins to increase sharply and reaches 0.92 at t = 4.5 h, reaching a plateau value of 0.94 that persists throughout polarization (5.6 < t (h) < 8.3). The second step commences shortly after Region III is fully

disordered, suggesting that the disordered phase propagates from the negative electrode towards the center of the cell, and at steady state the boundary between disorder and order resides in Region II. When the cell is switched to open circuit, the salt concentration gradient begins to relax, and the disordered regions give way to the equilibrium lamellar morphology. This disorder-to-order transition starts at the middle of the cell and propagates towards the negative electrode; Region II is completely ordered by $t = 18.1$ h, at which point Region III begins to transition from disorder to order. By $t = 22.1$ h the entire sample is ordered with $f_{DIS} = 0.30$; an indication that the current induced phase transitions are completely reversible. The subtle differences in f_{DIS} in the three regions prior to polarization are not seen at $t = 25.2$ h.

Measurement of the domain spacing as a function of time and position provides insight into the effect of polarization on molecular length scales; the data in Figure 1b allows us to make inferences about the local salt concentration based on measurements of the local domain spacing. We plot the time dependence of d_{LAM} (open symbols) and d_{DIS} (closed symbols) for the three regions in Figure 3d. Because the beam size is much larger than a single lamella (300 μm versus 8 nm), d_{LAM} represents an average over many lamellar grains. In general, $d_{LAM} > ¿7.55$ nm while $d_{DIS} < 7.55$ nm. This is consistent with the equilibrium properties of the electrolyte: the value of d at the equilibrium order-to-disorder transition is 7.55 nm (see Figure 1b). As the salt concentration in Region I increases, the lamellae near the positive electrode swell in response to an increase in the local salt concentration. $d_{LAM,I}$ increases from 7.55 nm to 7.63 nm while the cell is polarized and then remains more-or-less constant when the current is turned off. In Regions II and III, d_{LAM} is nearly independent of time. The data for $d_{LAM,III}$ is absent in Figure 3d between $2.2 < t$ (h) < 17.1 because the sample is completely disordered during this time window.

In Region III, polarization results in a decrease in salt concentration and the order-to-disorder transition as described by Figure 3c. Before polarization, the disordered phase coexists with ordered lamellae. The free energy required to place an LiTFSI molecule into a PEO-rich lamella is lower than that required to place it in a homogeneous PS/PEO mixture. Since the salt partitions to equate its chemical potential between the two phases, the local value of r in the disordered region must be less than that in the PEO-rich lamella, as required by the Gibbs phase rule. This is consistent with our observation that $d_{DIS,III}$ measured at the beginning of the experiment (7.37 nm) is lower than that of $d_{LAM,III}$ (7.55 nm) based on the mapping of d to r by Equation 1. At $t = 0.55$ h, the local value of r in the PEO-rich lamellae falls below the critical value needed to maintain phase separation and they become disordered, starting first at the bottom of Region III (depicted in Figure 1a) and propagating upward. At $t = 0.9$ h, $f_{DIS,III} = 0.55$ and Region III consists of a completely disordered morphology at the bottom (*i.e.*, closer to the negative electrode) and a lamellar phase in coexistence with a disordered phase at the top (*i.e.*, closer to the positive electrode). We refer to the neighboring ordered and disordered phases that are formed due the presence of ionic flux across the electrolyte as concurrent phases. It is important to distinguish between concurrent phases formed out of equilibrium (*e.g.* $t = 0.9$ h) and coexisting phases obtained at equilibrium due to the Gibb's phase rule (*e.g.* $t = -0.1$ h). The sharp increase of $d_{DIS,III}$ for $0.63 < t$ (h) < 1.8 is because the PEO-rich lamellae (prior to the order-to-disorder transition) have a higher local r than the coexisting disordered phase, and as the lamellae become disordered (*i.e.* mix the PS-rich domains), the amount of salt per ethylene oxide moiety in the disordered region must increase. At $t = 1.8$ h, the entirety of Region III is disordered and $d_{DIS,III} = 7.54$ nm. With no additional phase transitions occurring, $d_{DIS,III}$ begins to decrease as the local salt concentration continues to drop and the domain spacing plateaus at

$d_{DIS,III}$ = 7.40 nm by t = 6.0 h. This indicates that the salt concentration gradient has almost fully developed by this time. When the cell is switched to open circuit at t = 8.3 h, $d_{DIS,III}$ increases as the salt concentration gradient relaxes and the local salt concentration in Region III increases. At t = 18.6 h, we begin to observe the formation of a concurrent lamellar phase. Note that the ionic flux in the cell is not zero at this time even though the cell is at open circuit. With time, $f_{DIS,III}$ decreases and the equilibrium value of 0.30 is obtained at t = 23.0 h. The decrease in $d_{DIS,III}$ from t = 18.6 to 23.0 h is attributed to the partitioning of salt away from the disordered phase. For brevity, we do not include the data for $d_{DIS,I}$ and $d_{DIS,II}$ here but defer it to Figure S6 of the Supporting Information. Assuming the cell was at equilibrium at t = 0, we expect the cell to return to equilibrium at long times when $\Delta\Phi$ = 0 mV. It appears that equilibration of our sample requires longer times; $\Delta\Phi$ is 180 mV at 25.2 h, so it is not surprising that $d_{LAM,I}$ and $d_{DIS,III}$ at t = 25.2 h are different from those at t = 0 h.

We may use the measured domain spacing in Figure 3d to infer the local salt concentration as a function of $x L^{-1}$ and t based on the relationship between d and r_{avg} presented in Figure 1b. The mapping between d and r by Equation 1 (obtained from data in Figure 1b) requires accounting for the presence of both coexisting phases at equilibrium and concurrent phases when ionic flux is present. The value of d reported in Figure 1b based on the location of the primary scattering peak from ordered phases ignores the coexisting disordered phase. We thus rescale f_{DIS} given in Figure 3b to span from 0 to 1 and denote the rescaled volume fraction

f'_{DIS} (*i.e.* f'_{DIS} = 0 when f_{DIS} = 0.3 and f'_{DIS} = 1 when f_{DIS} = 1; $f'_{DIS} = \frac{1}{0.7}(f_{DIS} - 0.3)$). We

then calculate the local salt concentration, r_i, for each region (i = I, II, or III) by Equation 4 for each time point:

$$r_i = f'_{DIS,i} r_{DIS,i} + \left(1 - f'_{DIS,i}\right) r_{LAM,i} \tag{4}$$

where $r_{i,j}$ is the solution to Equation 1 (with r_{avg} replaced with $r_{i,j}$) which yields $d = d_{i,j}$ and j denotes LAM or DIS. In Figure 4a, we present the local salt concentration in Region I (red squares), Region II (green circles), and Region III (blue triangles) as a function of time. Initially, $r_i \approx 0.06$ in all three regions, which is slightly lower than the nominal value of $r_{avg} = 0.07$. The changes in local salt concentration in Regions I, II, and III during polarization are shown in Figure 4a. As expected, salt concentration increases in Region I with increasing time, remains more or less constant in Region II, and decreases in Region III. The average salt concentrations in the different regions at the end of polarization are $r_I = 0.090$ ($x L^{-1} = 0.26$), $r_{II} = 0.059$ ($x L^{-1} = 0.50$), and $r_{III} = 0.028$ ($x L^{-1} = 0.74$). We note that the average salt concentration in Region I cannot be much higher than 0.09 because the salt in Region I must come from Regions II and III and the average salt concentration throughout the electrolyte is fixed at $r_{avg} = 0.07$. This analysis relies on the assumption that the electrolyte morphology under applied electric fields at a given local salt concentration is identical to that obtained at equilibrium in individual electrolytes cast at the same salt concentration.
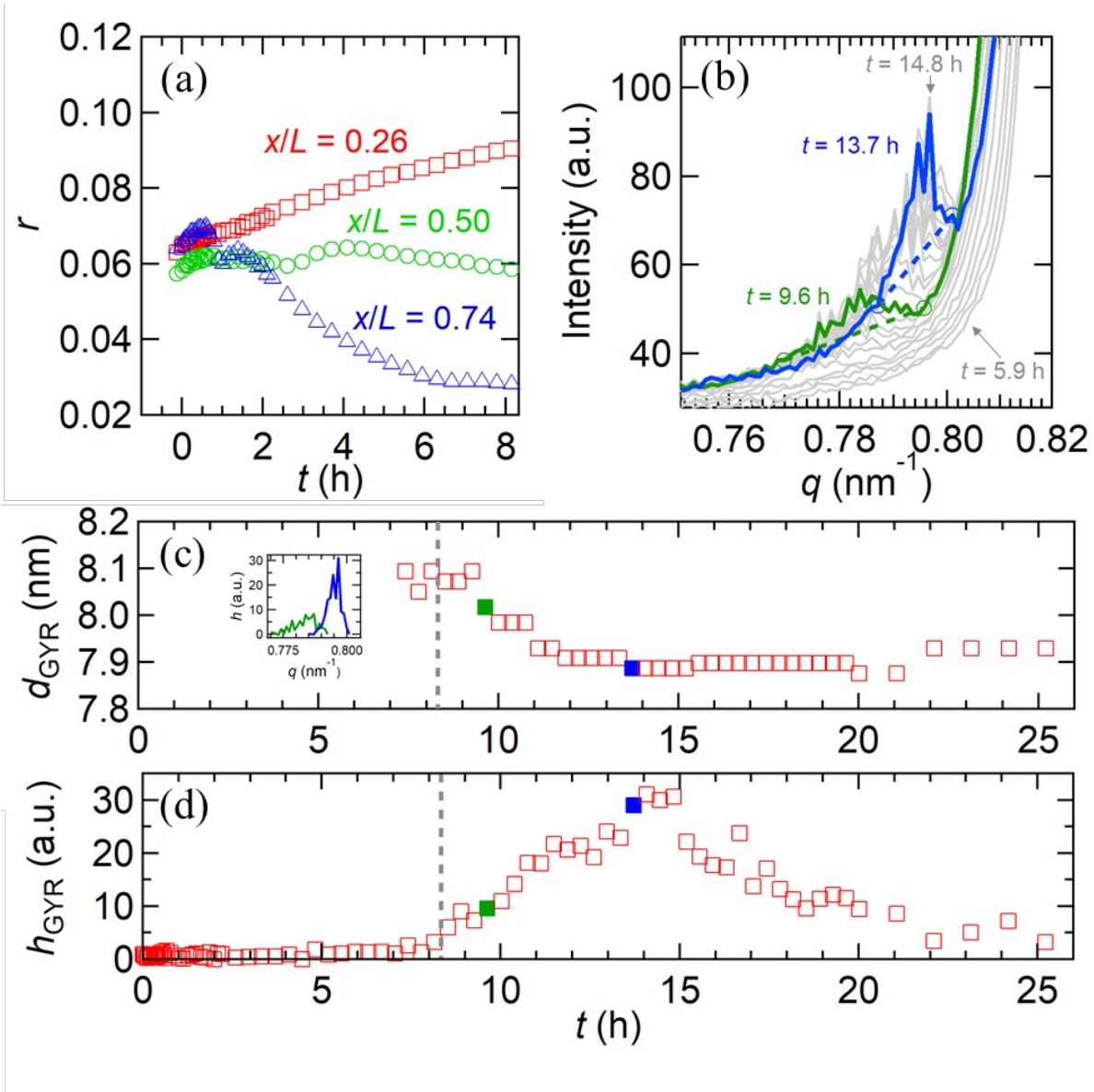
Figure 4. (a) Estimated local salt concentration in Region I (red squares), Region II (green circles), and Region III (blue triangles) versus time, t, based on Equation 4. (b) 1D scattering profiles obtained from Region I at t = 9.6 h (green curve) and t = 13.7 h (blue curve). The dashed lines represent a linear baseline. Gray curves represent the scattering data from t = 5.9 (when no gyroid peak is present) to t = 14.8 h (when the height of the peak is maximum). (c) Domain spacing of the gyroid phase, d_{GYR}, versus t. The inset shows the scattering data from t = 9.6 h (green curve) and t = 13.7 h (blue curve) after subtracting the linear baseline shown in Figure 4b. The maximum value for each curve was taken to be h_{GYR}, and the position of the maximum was used to calculate d_{GYR}. (d) Height of the gyroid peak, h_{GYR} versus t. The green and blue filled symbols in (c) and (d) correspond to the data at t = 9.6 and 13.7 h, respectively.

23

Emergence of the Gyroid Phase

We now discuss the formation of a gyroid phase which gives rise to the spots of high scattering intensity seen in Figure 2b on either side of the primary scattering ring. In Figure 4b, the gray curves represent the 1D scattering profiles obtained from selectively averaging the sectors of the 2D scattering imaging highlighted in Figure 2b for data obtained from Region I between $t = 5.9$ and $t = 14.8$ h for $0.75 < q$ $(nm^{-1}) < 0.82$. At early times, there is no feature corresponding to the gyroid phase; *i.e.*, the $t = 5.9$ h data set has no noticeable peak. As the experiment proceeds, a peak begins to emerge at $q = 0.77$ nm^{-1} which grows with time and shifts to higher q. The green ($t = 9.6$ h) and blue ($t = 13.7$ h) data sets in Figure 4b show two examples of scattering data with noticeable gyroid peaks. The location and intensity of the peak provide information on the nature of the current-induced gyroid phase. The measured scattering curves are corrected for scattering from the lamellar phase by subtracting linear baselines shown as dashed lines for the two examples in Figure 4b. We define the height of the peak, h_{GYR}, as the maximum intensity of the baseline corrected data and $q_{GYR}^{¿}$ to be the location of h_{GYR} on the q-

axis. We calculate the periodic length scale of the gyroid phase, $d_{GYR} = \dfrac{2\pi}{q_{GYR}^{¿}}$. The time dependence of d_{GYR} and h_{GYR} are presented in Figs 4c and 4d, respectively. Examples of background subtracted intensity profiles are shown in the inset of Figure 4c for the $t = 9.6$ h (green curve) and $t = 13.7$ h (blue curve) data sets. The dashed gray line in Figure 4c and 4d represent $t = 8.3$ h when the cell was switched to open circuit. The gyroid phase emerges near the end of the polarization step.

The gyroid phase is the thermodynamically favored morphology for the SEO copolymer electrolyte when $r > 0.17$ (see Figure 1b). The appearance of a gyroid phase in our experiment is surprising because we have estimated the maximum salt concentration in Region I to be $r_I = 0.09$ (see Figure 4a) based on the domain spacing of the lamellar phase. The fact that the gyroid phase is announced by spots rather than rings in the SAXS patterns indicates that the current-induced transformation from lamellae to gyroid occurs in relatively few grains. The current-induced gyroid phase first appears at $t = 7.1$ h and $d_{GYR} = 8.1$ nm. This suggests that the salt concentration within the gyroid grains is $r = 0.19$ based on the characteristic domain spacing of the gyroid morphology under quiescent conditions (Figure 1b). The fraction of Region I occupied by the gyroid phase is extremely small at all times: the integrated intensity of the SAXS peaks associated with this phase amounts to 0.42% or less (see Figure S7; the value of 0.42% is an upper limit calculated at $t = 13.7$ h when h_{GYR} in near the maximum). Thus, the presence of a small volume fraction of a salt-dense gyroid phase does not significantly change our calculation of the average salt concentration in Region I presented in Fig. 4a.

The mechanism by which the gyroid phase forms in response to ionic current remains an open question, although it has been previously reported in an SEO/LiTFSI electrolyte of the same copolymer[7]. We posit that the gyroid phase nucleates in Region I at defects where PEO-rich lamellae orientated parallel to the electric field terminate in a wall of polystyrene. Ions are driven towards the positive electrode in the PEO-rich channel but cannot penetrate the polystyrene, and salt accumulates in a highly salt-dense pocket, *i.e.*, a salt concentration hotspot. This may result in a steep microscopic salt concentration gradient on the length scale of the grain size (smaller than 1 µm). Such grain boundaries are necessarily rare in an unaligned sample, so

we would expect only a few gyroid grains to emerge. When the cell is switched to open circuit (t = 8.3 h), the salt diffuses away from the pocket and d_{GYR} decreases to 7.9 nm by t = 14.1 h, suggesting a decrease in r within the gyroid from 0.19 to 0.17 over the first six hours of open circuit. The relaxation of the microscopic salt concentration gradient results in an increase in the volume of polymer around the pocket where r > 0.17, and a local lamellar to gyroid transition occurs. We thus observe an increase in h_{GYR} from 6 to 31 in the time window from t = 8.3 to 14.9 h. The decay of h_{GYR} from 31 towards 0 for t > 14.9 h reflects the reconversion of the gyroid grains to the lamellar phase as the local salt concentration falls below the critical value needed to maintain the gyroid (r = 0.17). As expected, d_{GYR} remains constant during this decay. The changes in the 2D SAXS profiles in Region I, particularly the non-monotonic changes in intensity of the gyroid scattering spots, can be clearly seen in the movie file "Region_I.avi" in the Supporting Information.

In a previous work, Mullin et al studied the same SEO copolymer with a salt concentration of r_{avg} = 0.085 under applied fields of 2.5 to 15 V mm^{-1} [7]. They described the formation of gyroidal grains with a continuous gradient in domain spacing, which the termed "gradient crystals". In our experiment, we observe gyroid grains with a single, time-dependent domain spacing at a much lower field of 500 mV mm^{-1}. This suggests that steeper microscopic concentration gradients that must form under higher potential gradients result in a gyroid phase with a continuously changing domain spacing.

The effect of grain structure and defect density on ionic conductivity in block copolymer electrolytes has been studied using ac impedance spectroscopy, and it understood that conductivity decreases as grain size increases (*i.e.*, number of defects decreases) in unaligned

samples[32,33]. This conclusion is based on ac impedance spectroscopy which is, by definition, carried out without inducing concentration gradients. Our interpretation of how the current-induced gyroid phase is formed in the SEO/LiTFSI electrolyte at 500 mV mm^{-1} suggests that defects and grain boundaries play a more dramatic role when dc potentials are applied. The formation of concentration hotspots and the concomitant steep microscopic concentration gradients is outside the scope of 1D models of ion transport that are currently used to model batteries[34,35]. The development of 2 or 3D models based on Newman's concentrated solution theory[12] that incorporate the nanostructure of the composite electrolyte may be illuminating. A complete understanding of ion transport in composite electrolytes will require consideration of these effects.

Conclusions

To summarize, we have revealed rich phase behavior in a block copolymer electrolyte near the lamellar order-to-disorder phase boundary during dc polarization and subsequent relaxation. During polarization, three morphologies are present concurrently with characteristic spacings which vary significantly as a function of both position and time: a pure disordered phase near the negative electrode, coexisting lamellar and disordered phases in the middle of the cell, and coexisting lamellar, disordered, and gyroid phases near the positive electrode. The observation of a gyroid phase is especially significant because it implies the presence of concentration hotspots. We hypothesize that steep microscopic concentration gradients can develop in the cell at defect sites where the non-conducting polystyrene phase blocks the flow of ions parallel to the electric field. Such effects are not captured by existing theories that describe ion transport in lithium batteries using 1D models[12]. The relaxation of the current induced gyroid

phase under open circuit conditions is non-monotonic due to the presence of microscopic concentration gradients. While ion transport in block copolymer electrolytes (and composite electrolytes in general) has been extensively studied both experimentally[14,36,37] and computationally[38,39], it is usually assumed that the structure remains fixed during polarization. We have shown that this is not the case for an SEO/LiTFSI electrolyte operating under practical conditions with significant concentration polarization. It seems obvious that the interplay between the dynamic nanostructure and ion transport will depend on parameters such as domain size, geometry, average salt concentration, and current density. The experiment described in this work serves as an example of how these complex relationships could be unraveled.

ASSOCIATED CONTENT

Supporting Information: Detailed materials and experimental methods; equations used for fitting SAXS data; domain spacing, height of gyroid peak, scattering invariant, and volume fraction calculations; quantification of anisotropy in 2D scattering patterns; picture of the electrochemical cell; SAXS data during 120 °C annealing; bulk and interfacial resistances of the cell; domain spacing of the disordered phase for Regions I and II; calculation of the gyroid phase volume fraction; tabulated fit parameters

Region_I.mov: Movie file showing the time evolution of the 2D SAXS profiles from Region I and the emergence of the salt-rich gyroid phase

ABBREVIATIONS

DIS	disordered phase
GYR	gyroid phase

I	X-ray sampling region corresponding to the beam position centered at $x\,L^{-1} = 0.24$
II	X-ray sampling region corresponding to the beam position centered at $x\,L^{-1} = 0.50$
III	X-ray sampling region corresponding to the beam position centered at $x\,L^{-1} = 0.74$
LAM	lamellar phase
LiTFSI	bis(trifluoromethylsulfonyl)amine lithium salt
PEO	poly(ethylene oxide)
PS	polystyrene
SAXS	small angle X-ray scattering
SEO	polystyrene-*block*-poly(ethylene oxide)

SYMBOLS

d	domain spacing, nm
f	volume fraction
f'	rescaled volume fraction
f_c	conducting phase (*i.e.* PEO/LiTFSI) volume fraction
h	peak height, arbitrary units of inverse length
i	current density, mA cm^{-2}
I	scattered intensity, arbitrary units of inverse length
L	distance between the electrodes, mm
q	scattering vector, nm^{-1}
q^{i}	scattering vector at the primary peak, nm^{-1}
Q	scattering invariant, arbitrary units of inverse length per volume
r	salt concentration, molar ratio of LiTFSI molecules to ether oxygens
r_{avg}	average r from $x\,L^{-1} = 0$ to 1 in the electrolyte

t	time, h
T	temperature, °C
T_{ODT}	order-to-disorder transition temperature, °C
x	spatial coordinate parallel to the path of ion motion, μm
y	spatial coordinate perpendicular to the path of ion motion, μm

GREEK

α	correction factor to obtain volume fraction from scattering invariants
Φ_a	potential at the anode, mV
Φ_c	potential at the cathode, mV
$\Delta\Phi$	cell potential drop, mV

AUTHOR INFORMATION

Corresponding Author

*E-mail: nbalsara@berkeley.edu

Notes

The authors declare no competing financial interest.

REFERENCES

(1)   Cheng, X.-B.; Zhang, R.; Zhao, C. -.; Zhang, Q. Toward Safe Lithium Metal Anode in Rechargeable Batteries: A Review. *Chem. Rev.* **2017**, *117* (15), 10403–10473.

(2)   Tikekar, M. D.; Choudhury, S.; Tu, Z.; Archer, L. A. Design Principles for Electrolytes and Interfaces for Stable Lithium-Metal Batteries. *Nat. Energy* **2016**, *1* (9), 16114.

(3)   Howell, D.; Boyd, S.; Cunningham, B.; Gillard, S.; Slezak, L.; Ahmed, S.; Bloom, I.; Burnham, A.; Hardy, K.; Jansen, A. N.; Nelson, P. A.; Robertson, D. C.; Stephens, T.; Vijayagopal, R.; Carlson, R. B.; Dias, F.; Dufek, E. J.; Michelbacher, C. J.; Mohanpurkar, M.; Scoffield, D.; Shirk, M.; Tanim, T.; Keyser, M.; Kreuzer, C.; Li, O.; Markel, A.; Meintz, A.; Pesaran, A.; Santhanagopalan, S.; Smith, K.; Wood, E.; Zhang, J. Enabling Fast Charging – A Technology Gap Assessment. *J. Power Sources* **2017**, *367*, 250–262.

(4)   Pandian, A. S.; Chen, X. C.; Chen, J.; Lokitz, B. S.; Ruther, R. E.; Yang, G.; Lou, K.; Nanda, J.; Delnick, F. M.; Dudney, N. J. Facile and Scalable Fabrication of Polymer-Ceramic Composite Electrolyte with High Ceramic Loadings. *J. Power Sources* **2018**, *390*, 153–164.

(5)   Soo, P. P.; Huang, B.; Jang, Y. I. I.; Chiang, Y. M.; Sadoway, D. R.; Mayes, A. M. Rubbery Block Copolymer Electrolytes for Solid-State Rechargeable Lithium Batteries. *J. Electrochem. Soc.* **1999**, *146* (1), 32–37.

(6)   He, R.; Kyu, T. Effect of Plasticization on Ionic Conductivity Enhancement in Relation to Glass Transition Temperature of Crosslinked Polymer Electrolyte Membranes. *Macromolecules* **2016**, *49* (15), 5637–5648.

(7)   Mullin, S. A.; Stone, G. M.; Teran, A. A.; Hallinan, D. T.; Hexemer, A.; Balsara, N. P. Current-Induced Formation of Gradient Crystals in Block Copolymer Electrolytes. *Nano Lett.* **2012**, *12* (1), 464–468.

(8)   Teran, A. A.; Balsara, N. P. Thermodynamics of Block Copolymers with and without Salt. *J. Phys. Chem. B* **2014**, *118* (1), 4–17.

(9)   Gunkel, I.; Thurn-Albrecht, T. Thermodynamic and Structural Changes in Ion-Containing Symmetric Diblock Copolymers: A Small-Angle X-Ray Scattering Study. *Macromolecules* **2012**, *45* (1), 283–291.

(10)   Epps, T. H.; Bailey, T. S.; Waletzko, R.; Bates, F. S. Phase Behavior and Block Sequence Effects in Lithium Perchlorate-Doped Poly(Isoprene-b-Styrene-b-Ethylene Oxide) and Poly(Styrene-b-Isoprene-b-Ethylene Oxide) Triblock Copolymers. *Macromolecules* **2003**, *36* (8), 2873–2881.

(11)   Loo, W. S.; Galluzzo, M. D.; Li, X.; Maslyn, J. A.; Oh, H. J.; Mongcopa, K. I.; Zhu, C.; Wang, A. A.; Wang, X.; Garetz, B. A.; Balsara, N.P. Phase Behavior of Mixtures of Block Copolymers and a Lithium Salt. *J. Phys. Chem. B* **2018**, 122 (33), 8065–8074.

(12)   Newman, J.; Thomas-Alyea, K. E. *Electrochemical Systems*; Wiley, **2004**.

(13)   Villaluenga, I.; Pesko, D. M.; Timachova, K.; Feng, Z.; Newman, J.; Srinivasan, V.; Balsara, N. P. Negative Stefan-Maxwell Diffusion Coefficients and Complete Electrochemical Transport Characterization of Homopolymer and Block Copolymer Electrolytes. *J. Electrochem. Soc.* **2018**, *165* (11), A2766–A2773.

(14)   Galluzzo, M. D.; Loo, W. S.; Wang, A. A.; Walton, A.; Maslyn, J. A.; Balsara, N. P. Measurement of Three Transport Coefficients and the Thermodynamic Factor in Block Copolymer Electrolytes with Different Morphologies. *J. Phys. Chem. B* **2020**, *124* (5), 921–935.

(15)   Hexemer, A.; Bras, W.; Glossinger, J.; Schaible, E.; Gann, E.; Kirian, R.; MacDowell, A.; Church, M.; Rude, B.; Padmore, H. A SAXS/WAXS/GISAXS Beamline with Multilayer Monochromator. *J. Phys. Conf. Ser.* **2010**, *247* (1), 012007.

(16)   Teran, A. A.; Mullin, S. A.; Hallinan, D. T.; Balsara, N. P. Discontinuous Changes in Ionic Conductivity of a Block Copolymer Electrolyte through an Order–Disorder Transition. *ACS Macro Lett*. **2012**, *1* (2), 305–309.

(17)   Rey, I.; Bruneel, J.; Grondin, J.; Servant, L.; Lassègues, J. Raman Spectroelectrochemistry of a Lithium/Polymer Electrolyte Symmetric Cell. *J. Electrochem. Soc.* **1998**, *145* (9), 3034.

(18)   Steinrück, H.-G.; Takacs, C. J.; Kim, H.-K.; Mackanic, D. G.; Holladay, B.; Cao, C.; Narayanan, S.; Dufresne, E. M.; Chushkin, Y.; Ruta, B.; Zontone, F.; Will, J.; Borodin, O.; Sinha, S. K.; Srinivasan, V.; Toney, M. F. Concentration and Velocity Profiles in a Polymeric Lithium-Ion Battery Electrolyte. *Energy Environ. Sci.* **2020**, Advance Article.

(19)   Krachkovskiy, S. A.; Bazak, J. D.; Werhun, P.; Balcom, B. J.; Halalay, I. C.; Goward, G. R. Visualization of Steady-State Ionic Concentration Profiles Formed in Electrolytes during Li-Ion Battery Operation and Determination of Mass-Transport Properties by in Situ Magnetic Resonance Imaging. *J. Am. Chem. Soc.* **2016**, *138* (25), 7992–7999.

(20)   Zhou, J.; Danilov, D.; Notten, P. H. L. A Novel Method for the In Situ Determination of Concentration Gradients in the Electrolyte of Li-Ion Batteries. *Chem. - A Eur. J.* **2006**, *12* (27), 7125–7132.

(21)   Gomez, E. D.; Panday, A.; Feng, E. H.; Chen, V.; Stone, G. M.; Minor, A. M.; Kisielowski, C.; Downing, K. H.; Borodin, O.; Smith, G. D.; Balsara, N.P. Effect of Ion Distribution on Conductivity of Block Copolymer Electrolytes. *Nano Lett.* **2009**, *9* (3), 1212–1216.

(22)   Gartner, T. E.; Morris, M. A.; Shelton, C. K.; Dura, J. A.; Epps, T. H. Quantifying Lithium Salt and Polymer Density Distributions in Nanostructured Ion-Conducting Block Polymers. *Macromolecules* **2018**, 51 (5), 1917–1926.

(23)   Nakamura, I.; Wang, Z. G. Salt-Doped Block Copolymers: Ion Distribution, Domain Spacing and Effective χ Parameter. *Soft Matter* **2012**, *8* (36), 9356–9367.

(24)   Galluzzo, M. D.; Halat, D. M.; Loo, W. S.; Mullin, S. A.; Reimer, J. A.; Balsara, N. P. Dissolution of Lithium Metal in Poly(Ethylene Oxide). *ACS Energy Lett.* **2019**, *4* (4), 903–907.

(25)   Vigild, M. E.; Almdal, K.; Mortensen, K.; Hamley, I. W.; Fairclough, J. P. A.; Ryan, A. J. Transformations to and from the Gyroid Phase in a Diblock Copolymer. *Macromolecules* **1998**, *31* (17), 5702–5716.

(26)   Förster, S.; Khandpur, A. K.; Zhao, J.; Bates, F. S.; Hamley, I. W.; Ryan, A. J.; Bras, W. Complex Phase Behavior of Polyisoprene-Polystyrene Diblock Copolymers Near the Order-Disorder Transition. *Macromolecules* **1994**, *27* (23), 6922–6935.

(27)   Thelen, J. L.; Teran, A. A.; Wang, X.; Garetz, B. A.; Nakamura, I.; Wang, Z. G.; Balsara, N. P. Phase Behavior of a Block Copolymer/Salt Mixture through the Order-to-Disorder Transition. *Macromolecules* **2014**, *47* (8), 2666—2673.

(28)   Leibler, L. Theory of Microphase Separation in Block Copolymers. *Macromolecules* **1980**, *13* (6), 1602–1617.

(29)   Gibbs, J. W. On the Equilibrium of Heterogeneous Substances. *Trans. Connect. Acad. Arts Sci.* **1876**, *3*, 108–524.

(30) Nakamura, I.; Balsara, N. P.; Wang, Z. G. First-Order Disordered-to-Lamellar Phase Transition in Lithium Salt-Doped Block Copolymers. *ACS Macro Lett.* **2013**, *2* (6), 478–481.

(31) Roe, R. J. *Methods of X-Ray and Neutron Scattering in Polymer Science*; Oxford University Press, **2000**.

(32) Chintapalli, M.; Timachova, K.; Olson, K. R.; Mecham, S. J.; Devaux, D.; Desimone, J. M.; Balsara, N. P. Relationship between Conductivity, Ion Diffusion, and Transference Number in Perfluoropolyether Electrolytes. *Macromolecules* **2016**, *49* (9), 4508—3515.

(33) Kambe, Y.; Arges, C. G.; Czaplewski, D. A.; Dolejsi, M.; Krishnan, S.; Stoykovich, M. P.; De Pablo, J. J.; Nealey, P. F. Role of Defects in Ion Transport in Block Copolymer Electrolytes. *Nano Lett.* **2019**, *19* (7), 4684–4691.

(34) Doyle, M.; Fuller, T. F.; Newman, J. Modeling of Galvanostatic Charge and Discharge of the Lithium/Polymer/Insertion Cell. *J. Electrochem. Soc.* **1993**, *140* (6), 1526–1533.

(35) Kim, H.-K.; Balsara, N. P.; Srinivasan, V. Continuum Description of the Role of Negative Transference Numbers on Ion Motion in Polymer Electrolytes. *J. Electrochem. Soc.* **2020**, *167*, 110559.

(36) Panday, A.; Mullin, S.; Gomez, E. D.; Wanakule, N.; Chen, V. L.; Hexemer, A.; Pople, J.; Balsara, N. P. Effect of Molecular Weight and Salt Concentration on Conductivity of Block Copolymer Electrolytes. *Macromolecules* **2009**, *42* (13), 4632—4637.

(37) Young, W. S.; Epps, T. H. Ionic Conductivities of Block Copolymer Electrolytes with Various Conducting Pathways: Sample Preparation and Processing Considerations. *Macromolecules* **2012**, *45* (11), 4689–4697.

(38) Shen, K.-H.; Brown, J. R.; Hall, L. M. Diffusion in Lamellae, Cylinders, and Double Gyroid Block Copolymer Nanostructures. *ACS Macro Lett.* **2018**, *7* (9), 1092–1098.

(39) Shen, K.-H.; Hall, L. M. Ion Conductivity and Correlations in Model Salt-Doped Polymers: Effects of Interaction Strength and Concentration. *Macromolecules* **2020**, *53* (10), 3655—3668.

Table of Contents Graphics